

Reconfigurable, non-volatile control of optical anisotropy in ReS₂ via ferroelectric gating

Mahfujur Rahaman^{1,†}, Seunguk Song^{1,2,3,†,*}, Aaliyah C. Khan⁴, Bongjun Choi¹, Aaron M. Schankler⁴, Kwan-Ho Kim¹, Wonchan Lee^{2,3}, Jason Lynch¹, Hyeon Suk Shin^{3,5}, Andrew M. Rappe⁴, and Deep Jariwala^{1,*}

¹*Department of Electrical and Systems Engineering, University of Pennsylvania, Philadelphia, Pennsylvania 19104, United States*

²*Department of Energy Science, Sungkyunkwan University (SKKU), Suwon 16419, Republic of Korea*

³*Center for 2D Quantum Heterostructures (2DQH), Institute for Basic Science (IBS), Suwon 16419, Republic of Korea*

⁴*Department of Chemistry, University of Pennsylvania, Philadelphia, Pennsylvania 19104, USA.*

⁵*Department of Chemistry, Sungkyunkwan University (SKKU), Suwon, 16419, Republic of Korea*

[†]These authors contributed equally: Mahfujur Rahaman, Seunguk Song

*Correspondence should be addressed. Email to: seunguk@skku.edu (S.S.), dmj@seas.upenn.edu (D.J.)

ABSTRACT

Electrically tunable linear dichroism (LD) with non-volatile properties represents a critical yet elusive feature for next-generation integrated photonic elements in practical device architectures. Here, we demonstrate record-breaking, non-volatile control of optical anisotropy in two-dimensional ReS₂ via ferroelectric gating with aluminum scandium nitride (AlScN). Our ferroelectric field-effect transistors achieve near-unity ($\approx 95\%$) LD tunability of differential reflectance at room temperature—the highest reported for any electrically controlled 2D optical system. Crucially, the programmed optical states exhibit exceptional retention exceeding 12,000 seconds without applied bias, enabling true non-volatile optical memory. Through combined experimental characterization and *ab initio* calculations, we reveal that ferroelectric polarization switching induces substantial asymmetric charge transfer to ReS₂, selectively populating conduction band states and triggering structural distortions that dramatically enhance optical anisotropy in the "up" polarization state while leaving the "down" state unperturbed. This ferroelectric-semiconductor coupling provides a universal platform for voltage-programmable, energy-efficient photonic devices with dynamic polarization control, addressing critical needs in integrated photonics as well as programmable far-field optics and telecommunications infrastructure.

INTRODUCTION

Optical anisotropy—the directional dependence of light propagation through materials—underpins virtually all modern linear and non-linear photonic technologies, from liquid crystal displays to optical fiber communications and polarized optical imaging by serving as a central operating principle for polarizers, waveplates, and phase-matching elements¹⁻⁴. It arises from birefringence, which is the difference in refractive index parallel and perpendicular to a specific orientation axis. When light passes through a crystal with structural or electronic anisotropy along or across an orientation axis, it induces anisotropic light propagation, providing a means to control the polarization of light. Many conventional bulk materials, including liquid crystals⁵, polymers^{6,7}, metamaterials⁸, and oxides^{9,10}, are well known for their optical anisotropy and have been widely commercialized in polarized photonic devices¹¹⁻¹³. However, their three-dimensional (3D) bulk nature, rigidity, and limited active polarization control present significant challenges for integration into micro- or nano-scale devices¹⁴.

Two-dimensional (2D) van der Waals materials with intrinsic in-plane anisotropy have emerged as promising alternatives, offering atomically thin active layers with strong optical anisotropy¹⁵⁻¹⁹. Among them, ReS₂ is particularly compelling due to its distorted 1T' crystal structure featuring quasi-one-dimensional Re-Re chains that generate substantial linear dichroism (LD) along specific crystallographic axes²⁰⁻²². Despite extensive research demonstrating LD values up to 30% in pristine ReS₂, achieving dynamic, electrically controlled modulation has remained challenging²². Previous approaches using conventional gate dielectrics have achieved limited LD tunability (33-46%) in materials like black phosphorus, but critically require large, continuously applied voltages (± 80 V) for operation, making them impractical for low-power applications²³. More fundamentally, these electrostatic approaches provide only volatile control, i.e., the optical state is lost immediately when power is removed, precluding applications requiring optical memory or standby power elimination.

Ferroelectric gate dielectrics offer a transformative solution by providing switchable, remanent polarization that maintains electrostatic fields without continuous power consumption. Wurtzite-phase scandium-doped aluminum nitride (AlScN) represents an ideal ferroelectric gate material, combining exceptionally large remanent polarization ($P_r \approx 80-115 \mu\text{C}/\text{cm}^2$), full CMOS

compatibility, and demonstrated ability to induce carrier densities exceeding 10^{14} cm^{-2} in 2D channels²⁴⁻²⁷. Despite this potential, ferroelectric control of optical anisotropy in 2D materials has not been realized experimentally.

Here, we demonstrate the first non-volatile, electrically programmable control of optical anisotropy using ferroelectric-gated ReS₂. Our approach achieves record-high LD tunability ($\approx 95\%$) at room temperature with retention times exceeding 12,000 seconds, establishing non-volatile control of the fundamental optical property of LD. Through detailed *ab initio* modeling, we reveal the fundamental mechanism: asymmetric charge transfer induced by ferroelectric polarization switching that selectively modulates the electronic structure and atomic configuration of ReS₂. Our work opens pathways for voltage-programmable photonic systems with applications spanning optical computing, telecommunications, and polarized imaging.

RESULTS AND DISCUSSION

Ferroelectric gating in in-plane anisotropic ReS₂.

Figure 1a shows the schematic of a back-gated FeFET device architecture. We use ferroelectric AlScN (100 nm) on Pt/Si substrate as the gate dielectric. ReS₂ flakes are exfoliated from a commercially available bulk crystal and transferred onto the AlScN substrate prior to device fabrication. Details of the device fabrication can be found in the Experimental section. **Figure 1b** displays one of the FeFETs studied in this work. **Figure 1c** is a schematic of the ReS₂ crystal structure (top view). Single-layer ReS₂ consists of a plane Re atoms sandwiched between two S planes. However, unlike other TMDs, strong Re-Re covalent bonds favor conversion from the symmetric trigonal prismatic (2H) structure to antiprismatic (locally distorted ReS₆ octahedra, 1T") coordination, creating pseudo-1D Re-Re chains within the basal plane (along the *b*-axis).²² (shown by green arrow in **Fig. 1c**). As reported in the literature²⁸, light can be polarized parallel/perpendicular to this *b*-axis, giving rise to in-plane optical anisotropy.

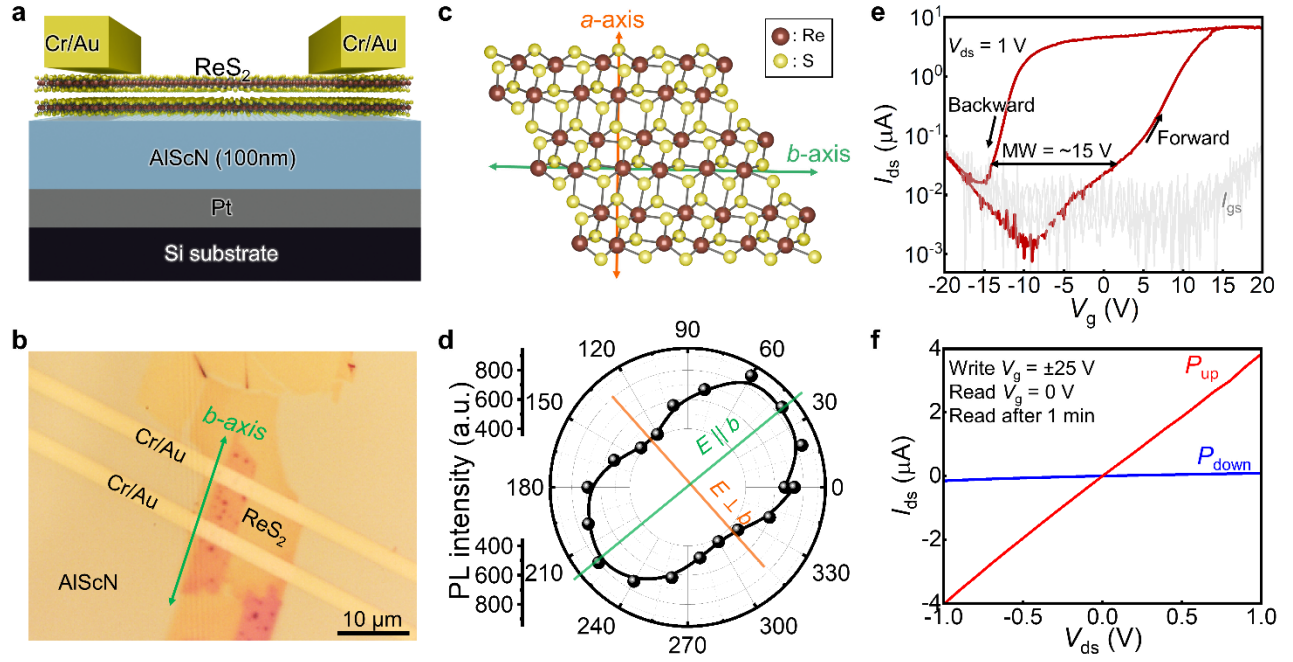


Figure 1. Non-volatile control of electrical conductivity and optical anisotropy of ReS₂. (a) Schematic of the back gate ferroelectric field-effect transistor (FeFET) device architecture showing ferroelectric AlScN on a Pt/Si substrate. ReS₂ flakes are exfoliated and then dry transferred onto the AlScN substrate prior to device fabrication. (b) Optical image of a representative ReS₂/AlScN FeFET. (c) Top-view schematic of the ReS₂ crystal structure. One-dimensional Re–Re (Red spheres) chains are aligned along the *b*-axis (green arrow), enabling in-plane optical anisotropy (S atoms: yellow). (d) Linearly-polarized photoluminescence (PL) spectrum of the ReS₂ device shown in (b) measured at room temperature. (e) Representative transfer curve of a ReS₂/AlScN FeFET illustrating a counterclockwise hysteresis loop with a memory window >15 V as the gate voltage (V_g) is swept. (f) Output curves for the polarization up (P_{up}) and down (P_{down}) states, recorded at $V_g = 0$ V after a ± 25 V pulse (applied for 1 s), demonstrating non-volatile and controllable channel conductance modulation.

Figure 1d presents linearly polarized PL results of the ReS₂ device on AlScN collected at room temperature. Raw PL data for these measurements can be found in **Figure S1**. The PL intensity follows a clear $\cos^2\theta$ dependence on the excitation polarization angle θ , defined as the angle between the incident electric-field vector (E) and the crystallographic *b*-axis^{22,29,30}. This behaviour reflects the fact that the transition-dipole moment of the lowest-energy excitons (X_1, X_2) is oriented nearly parallel to the Re–Re chain (*b*-axis); thus, when $E \parallel b$ -axis ($\theta \approx 40^\circ$ in **Fig. 1d**), the PL reaches its maximum, whereas rotating the polarization by 90° to $\theta \approx 130^\circ$ ($E \perp b$) suppresses the signal^{22,30}. The polarization angle that maximizes PL is therefore used as an experimental marker of the *b*-axis, and we set this direction as the reference for all subsequent

measurements. As a note, for each device we collect polarized PL separately to determine the b -axis of the ReS₂ flake prior to conducting gate-controlled LD experiments. Additionally, we use PL measurement primarily to determine the thickness of the flake, as reported in the literature. One such thickness determination of ReS₂ flakes can be found in **Fig. S1**. Note that, similar to other 2D TMDs, ReS₂ exhibits layer-dependent bandgap (1.4 eV in the bulk to 1.7 eV for the monolayer³¹); however, owing to its weak interlayer coupling, its bandgap remains direct at all thicknesses.

A representative transfer curve of a ReS₂/AlScN FeFET is shown in **Fig. 1e**. As the gate voltage (V_g) is swept from -20 V to $+20$ V, the channel drain-source current (I_{ds}) changes as the electrical conductivity transitions from the OFF state to the ON state. Furthermore, when V_g is swept in the opposite direction from $+20$ V to -20 V, the high electrical conductivity is maintained until about -5 V, after which it enters the OFF state again. Therefore, the hysteresis loop of the transfer curve is drawn in a counterclockwise direction, which is typical of FeFET behavior due to ferroelectric gating. The shift in threshold voltage, i.e., memory window (MW), is found to be > 15 V during the DC V_g sweep. For AlScN, when V_g is applied sufficiently negatively (e.g., $V_g = -20$ V), the ferroelectric polarization inside the AlScN directs downward (P_{down}); conversely, when V_g is applied sufficiently positively (e.g., $V_g = +20$ V), the polarization switches upwards (P_{up}), changing the channel conductance. **Figure 1f** shows the output curve of the P_{up} and P_{down} states as V_g ($= \pm 25$ V applied for 1 s) is varied (i.e., programmed/erased) and measured at $V_g = 0$ V after 1 min. As can be seen, the channel conductance is nonvolatile and controllable depending on the P_{up} and P_{down} states.

Tunable optical anisotropy and its non-volatility

To demonstrate a programmable ferroelectric gate-tunable LD in ReS₂, we perform differential reflectance measurements on ReS₂-AlScN devices. **Figure 2a,b** present the linearly polarized optical response of the device shown in **Fig. 1b** under positive bias (switching the AlScN polarization upward, P_{up}) and negative bias (switching the polarization downward, P_{down}). Here, the green curve shows the response when incoming light is polarized along the ReS₂ b -axis, and

the red curve is for incoming light polarized perpendicular to the ReS₂ *b*-axis. Inset of **Fig. 2a** shows the configuration of initial light polarization and the direction of ReS₂ crystal *b*-axis. Details of the differential reflectance measurements and angle-dependent differential reflectance spectra of this device for P_{up} and P_{down} are displayed in **Fig. S2** and **S3**. LD is calculated using **Equation 1** below^{32,33}:

$$\frac{(\Delta R_{\text{par}} - \Delta R_{\text{per}})}{(\Delta R_{\text{par}} + \Delta R_{\text{per}})} \quad (1)$$

, where ΔR_{par} and ΔR_{per} are the differential intensities of polarized reflectance parallel and perpendicular to the ReS₂ *b*-axis, respectively. **Figure 2c,d** display the LD measured for P_{up} and P_{down} state, respectively. As can be seen, for the P_{up} state, we can achieve a very high degree of tunability, with LD above 95% for measurements performed at room temperature at the wavelength of 815 nm (band edge of ReS₂). Whereas, for the P_{down} state, LD is $\approx 20\%$ at the band edge. Although near-unity LD has been demonstrated in 2D NbOCl₂ through its intrinsic in-plane anisotropy in the ultraviolet regime³⁴ and in 2D antiferromagnetic FePS₃ via cavity enhancement in the visible spectrum³⁵, achieving on-chip LD that is electrically tunable has remained challenging. Our device overcomes this limitation by delivering similarly high LD that can be switched reversibly with a low gate bias.

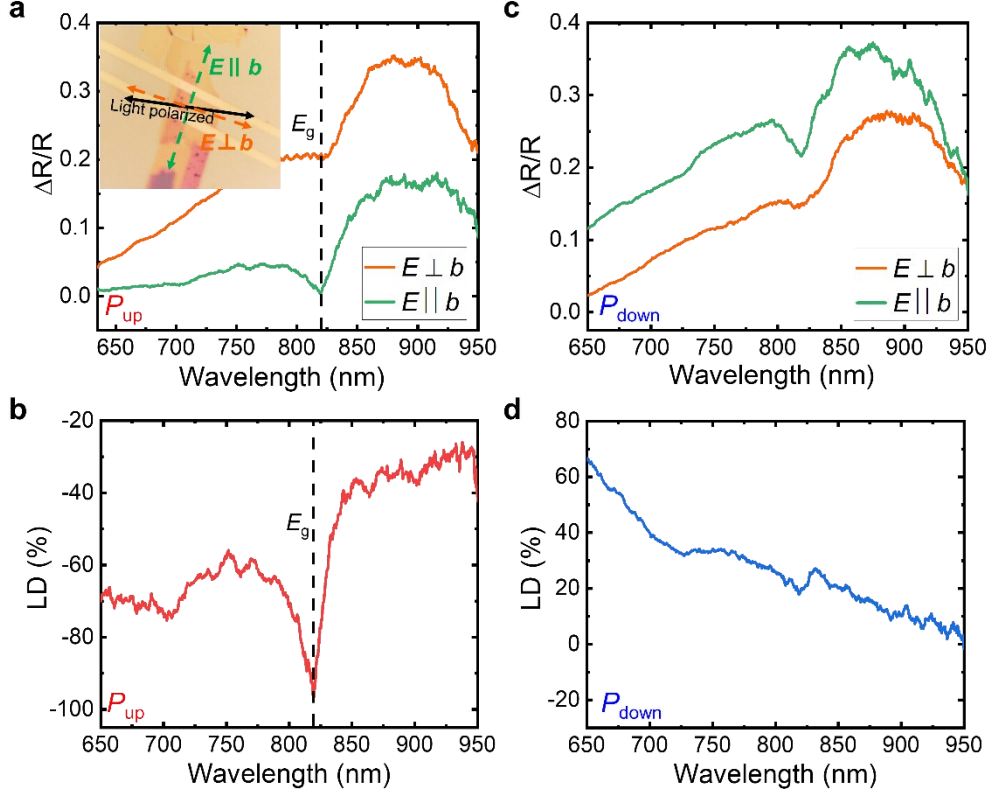


Figure 2. Linear dichroism (LD) of differential reflectance in ReS₂ controlled by AlScN at room temperature. (a, b) Differential reflectance spectra of the ReS₂/AlScN device (same as in Fig. 1b) under P_{up} and P_{down} state. In each panel, the green curve represents the signal when the incoming light is polarized along the ReS₂ b-axis, while the red curve corresponds to polarization perpendicular to the b-axis. The inset in (a) illustrates the configuration of the incident light polarization and the ReS₂ crystal b-axis. (c, d) LD under the P_{up} and P_{down} states, respectively. Notably, the P_{up} state exhibits a tunable LD of $\sim 95\%$ at room temperature at the ReS₂ band edge (815 nm), whereas the P_{down} state shows an LD of $\sim 20\%$.

To further validate our polarized optical response results, we conduct polarized PL measurements on our ReS₂/AlScN devices. **Figure 3a,b** shows the polarization-resolved PL spectrum of the ReS₂/AlScN device measured for ferroelectric gate switched ON/OFF states (P_{up} - P_{down}) measured at room temperature, respectively. The PL peak centered at ~ 820 nm (1.51 eV) with a weak shoulder around 780 nm (1.59 eV), a signature of the 5L structure of ReS₂ (see **Fig. S1**). To calculate the degree of linear polarization (DoLP) for PL, we use the equation,

$$\frac{(I_{par} - I_{per})}{(I_{par} + I_{per})} \quad (2)$$

, where I stands for PL intensity. As can be seen, PL spectrum collected parallel and perpendicular to the ReS₂ crystal b -axis in P_{up} state has higher DoLP with $\approx 44\%$ than P_{down} state with $\approx 31\%$, in qualitative agreement to the LD results presented in **Fig. 2**. We also confirm that this trend is reproducible in ReS₂ devices of different thicknesses, which show similar DoLP behavior between the P_{up} and P_{down} states (**Fig. S4**).

We also measure polarization-resolved PL spectra of the device for both P_{up} and P_{down} states at the lower temperature of ≈ 77 K. **Figure 3b,c** displays polarization-resolved normalized PL spectrum for the two ferroelectric switching states, respectively. At 77 K, we can clearly observe two distinct signature PL peaks of ReS₂ (labeled as X_1 and X_2 in **Fig. 3c,d**), both of which exhibit polarization dependency. For the P_{up} state, the DoLP parallel/perpendicular to the ReS₂ b -axis are determined to be $\approx 63\%$ for X_1 and $\approx 65\%$ for X_2 . By contrast, for the P_{down} state, these values are determined to be $\approx 39\%$ and $\approx 40\%$, respectively. A similar trend is also observed in a different device, confirming its reproducibility (**Fig. S6**). As a control experiment, we also measure polarization-resolved PL spectra of ReS₂ on a SiO₂/Si substrate and compared with the ReS₂/AlScN device before and after polarization switching (**Fig. S7**). The DOLP of ReS₂ on the AlScN substrate ($\approx 44\%$ for X_1 even before bias) is higher than that observed in the ReS₂ crystal on SiO₂ ($\approx 32\%$ for X_1), which is attributed to the intrinsic net positive polarization (partial P_{up}) of AlScN even before initial poling^{24,36} (see **Fig. S7**).

We also observe a stable retention time for the DOLP exceeding 12,000 seconds for both the P_{up} and P_{down} states, measured at 77 K (**Fig. 3e**). These findings hold significant promise for non-volatile optoelectronic memory devices that encode both electrical conductance and emission/extinction polarization. This extended retention time is primarily attributed to the robustness of the ferroelectric polarization state. For example, this long retention is confirmed by the excellent retention of the FeFET channel drain-source current (I_{ds}), indicating that once the P_{up} and P_{down} state is written, they remain stable (**Fig. 3f**). Importantly, such long-lived preservation of polarization-resolved optical signals is rarely achieved in anisotropic 2D materials, marking a critical step toward electrically programmable, optically readable non-volatile functionalities in hybrid ferroelectric/2D platforms.

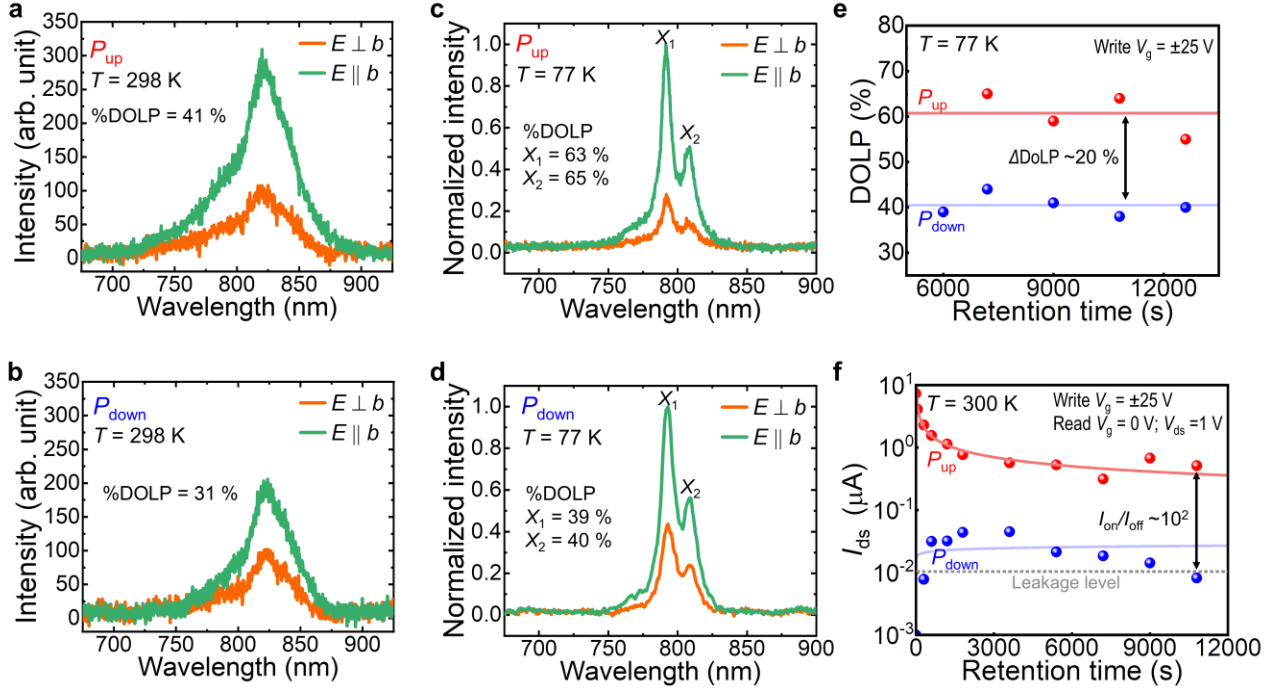


Figure 3. Polarization-resolved PL spectroscopy and their retention. (a, b) Room-temperature polarization-resolved PL spectra of the ReS₂/AlScN FeFET for the (a) P_{up} and (b) P_{down} states. The degree of linear polarization (DoLP) is $\approx 44\%$ for the P_{up} state and $\approx 31\%$ for the P_{down} state. (c, d) Normalized polarization-resolved PL spectra measured at ≈ 77 K for the (c) P_{up} and (d) P_{down} states. Two distinct PL peaks, labeled X_1 and X_2 , are clearly observed, each exhibiting strong polarization dependence. For the P_{up} state, the DoLP is $\approx 63\%$ for X_1 and $\approx 65\%$ for X_2 , whereas for the P_{down} state these values decrease to $\approx 39\%$ and $\approx 40\%$, respectively. (e) Polarization-resolved PL measurements reveal a stable retention time for the DOPL measured at 77 K. (f) FeFET channel read current (I_{ds}) retention, indicating robust stability of the programmed P_{up} and P_{down} states.

Theoretical analysis of the interface

A simplified model of the device architecture is used to theoretically model the charge transfer and structural properties of a $\text{ReS}_2/\text{AlN}/\text{Pt}$ interface. Factors considered when designing the model system are discussed in **Supplementary Note S1**. The relaxed geometries, the k -resolved electronic band structures, and the projected density of states of the interfaces are shown in **Fig. 4**. The band structure and density of states reveal that the $P_{\text{up}}/P_{\text{down}}$ interfaces passivate the polar AlN using different mechanisms. In the P_{up} interface, the ReS_2 and AlN have a strong charge transfer interaction, as seen through the closer distance between the layers in the relaxed structure (**Fig. 4c, f**). Examination of the electronic structure shows corresponding behavior, where additional charge accumulates in the ReS_2 to passivate the polarization of the AlN substrate. This can be seen in the band structure (**Fig. 4a**), where the lowest conduction band of ReS_2 is completely filled by this charge accumulation, and the projected density of states (PDOS) shows that this charge localizes primarily on the Re atoms of the lower ReS_2 layer (**Fig. 4b**, and **Fig. S7**), while the layer of ReS_2 farther from the interface remains unaffected. The layer projected density of states (**Fig. S8, 9**) suggests that the charge accumulation in the ReS_2 layer helps screen the AlN depolarization field in the P_{up} interface, but because the lowest ReS_2 conduction band is energetically separated from the higher conduction bands, the passivation is incomplete.

On the other hand, the P_{down} interface shows no major charge transfer to the ReS_2 conduction band (**Fig. 4d**). Instead, the electronic structure near the Fermi level is composed primarily of N orbitals (**Fig. 4e**), indicating that holes accumulate on the top AlN surface and that ReS_2 is not involved in passivation. In the P_{down} case, the terminating N layer primarily binds holes, and the ReS_2 does not significantly stabilize holes to screen the depolarizing field. This shows that the polarization state of the AlN substrate can have a significant impact on the electronic properties of the adjacent ReS_2 layer, with the lowest conduction band (CBM) being the most strongly affected.

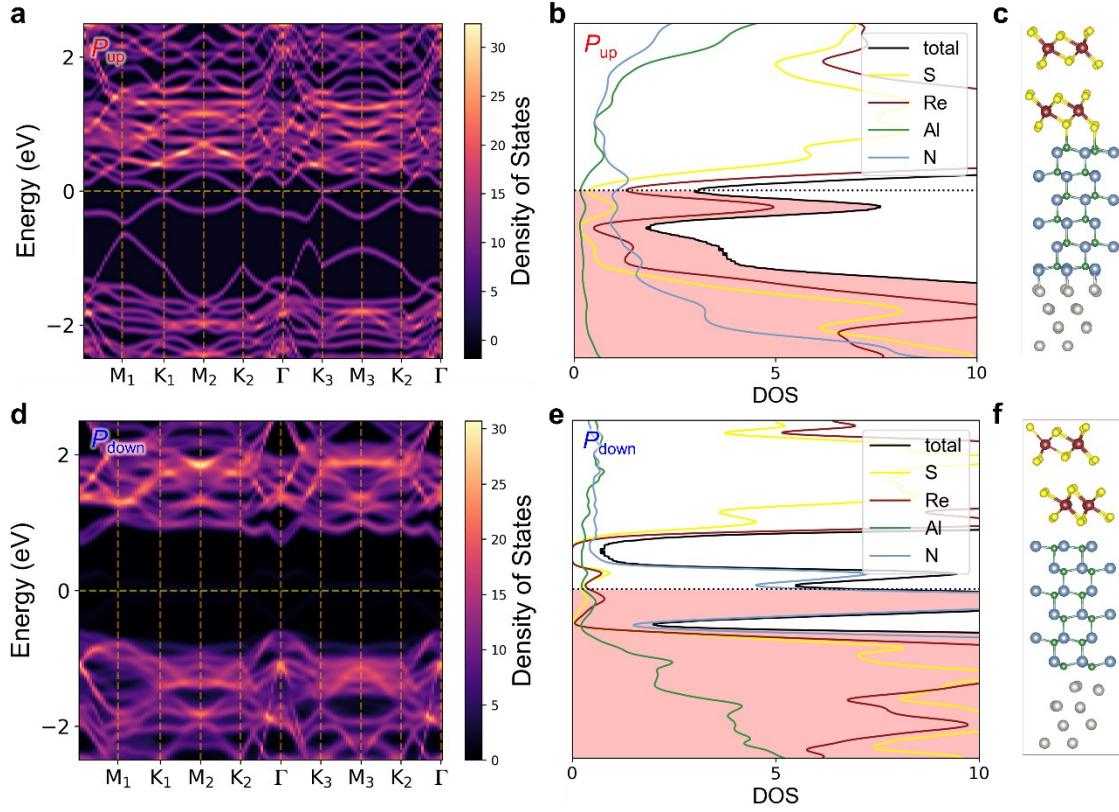


Figure 4. Electronic properties of the interface structures. (a, d) k -resolved density of states projected on ReS₂ orbitals for (a) P_{up} and (d) P_{down} model interfaces. The Fermi level is set to zero and is indicated by a dashed yellow line. (b, e) Projected density of states for (b) P_{up} and (e) P_{down} showing the total orbital contribution of each atomic species. The Fermi level is marked by a black dashed line. (c, f) Relaxed geometry of the (c) P_{up} and (d) P_{down} model interfaces (Re: red, S: yellow, Al: green, N: blue, Pt: gray).

To investigate the effects of charge transfer in the P_{up} interface on the electronic properties of ReS₂, the band structure of the ReS₂ bilayer is calculated. This is done by calculating the electronic structure (Fig. 5a) while preserving the ground state atomic positions of the ReS₂ bilayer from the interface (Fig. 5b). While the ReS₂ structure in the P_{down} interface is barely affected (Fig. S9), reflecting its weak interaction with the ferroelectric substrate, the lowest layer of ReS₂ in the P_{up} interface undergoes more significant deformation. Here, one out of the two Re–Re pairs in the unit cell separates and the Re atoms move in opposite directions along the a -axis. The band structure shows that the CBM is most strongly affected by this distortion (Fig. 4a), and the wavefunction corresponding to this band exhibits an anti-bonding character localized on the displaced Re atoms. Peierls distortions have been previously recognized as critical in stabilizing

electronic bands in ReS_2 ^{31,37}, ultimately leading to the formation of the zigzag Re–Re chains along the b -axis and the further formation of four-atom diamond shaped clusters. Charge filling of CBM in the P_{up} interface populates anti-bonding states that leads to the ordered dissociation of one pair of Re atoms in adjacent clusters enhancing the Peierls distortion. These insights can be further used to understand the ferroelectric polarization-dependent optical responses for other anisotropic materials.

To connect the structural distortions and charge transfer processes experienced by ReS_2 in the interfaces to the optical anisotropy observed in the experiments, we calculate the imaginary dielectric response function of the isolated, distorted ReS_2 bilayer (**Fig. 5d-f**). The AlN and Pt layers were deleted, keeping only ReS_2 with the charge-induced structural distortions. We make this approximation since the energy range of interest falls within the bandgap of AlN (≈ 4 eV calculated), and the Pt substrate primarily serves as an electronic reservoir. Moreover, the removal of AlN and Pt resets the charge state of ReS_2 with an unfilled CBM. In the interface model, the CBM is fully occupied (**Fig 5a-b**). However, experimental reflectance spectra show that the bandgap of ReS_2 in P_{up} vs. P_{down} is relatively unchanged (**Fig. 2**), suggesting that the electronic occupations are not changed enough to allow new optical transitions out of the CBM. This implies that the CBM is only partially filled in the experimental interface, destabilizing the atomic structure but not significantly perturbing the electronic structure. To simulate this, after removal of the AlN and Pt layers, we fix the occupations of the ReS_2 so that the conduction band remains empty. Thus, we consider transitions into the CBM and emphasize these transitions as the most important for determining the difference in the optical properties between P_{up} and P_{down} .

The dielectric response is computed along two directions: the b -axis (parallel to Re chain direction) and the cross direction (perpendicular to the b -axis). The results shown in **Fig. 5d-f** reveal anisotropy in the contribution to the dielectric response from the CBM. However, the direction of the anisotropy in the P_{down} and P_{up} structures is different. The P_{up} dielectric function exhibits a large early onset peak (**Fig. 5d**) where the parallel dielectric response is greater than the perpendicular response. In contrast, the P_{down} and pristine bilayers show a larger contribution from the perpendicular response compared to the parallel response. This shows that the structural and

electronic changes induced by the charge accumulation in the ReS_2 play a central role in the determination of the optical properties.

To sum up, in the P_{up} interface, charge accumulates in the ReS_2 in order to passivate the ferroelectric substrate, populating the Re orbitals and perturbing the atomic structure. Conversely, in the P_{down} interface, ReS_2 does not play a role in screening the depolarizing field. The population of the conduction band of ReS_2 in the P_{up} interface contributes to distortions of the Re atoms along the b -axis. The changes to the ReS_2 atomic structure introduced by this distortion affect the anisotropy of the optical response. These insights provide a framework for engineering the anisotropic optical properties of ReS_2 and similar materials, enabling the fine-tuning of device responses through polarization state control.

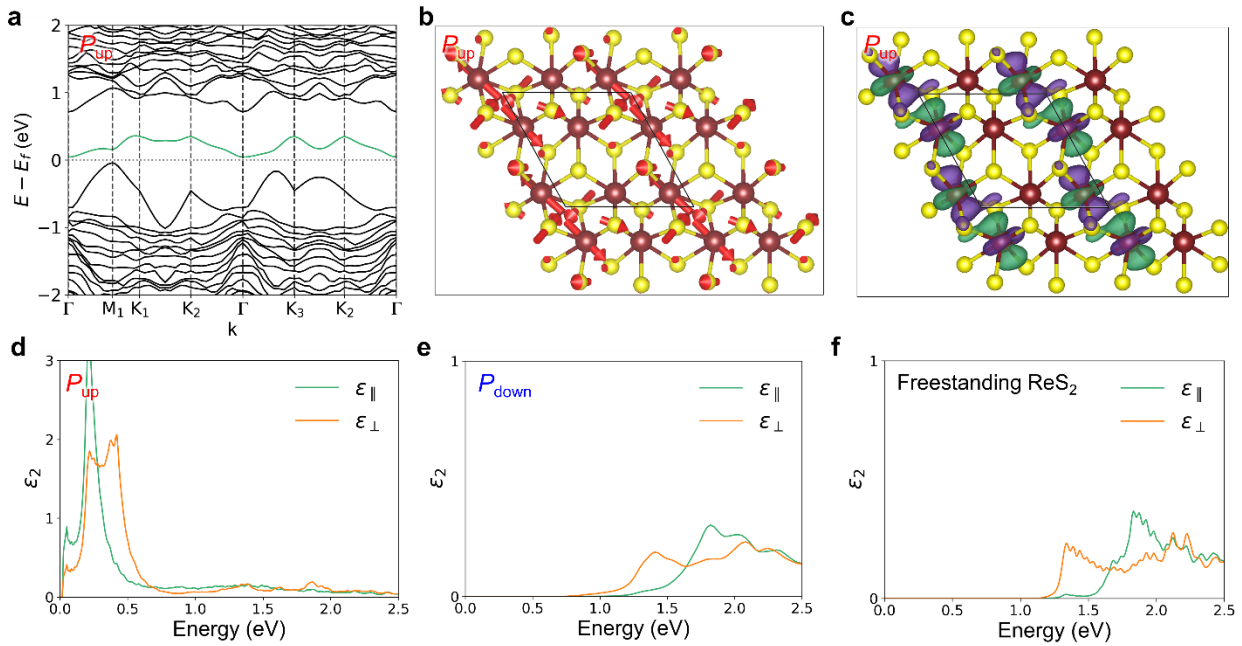


Figure 5. Theoretical analysis on optical response of ReS_2 . (a-c) Theoretical analysis on charge induced distortion in P_{up} interface. (a) Electronic band structure of the ReS_2 bilayer with structural distortions from P_{up} interface highlighting the lowest conduction band (CBM) in green. (b) In-plane view (Re: red, S: yellow) of displacement pattern of the lowest ReS_2 layer in the P_{up} interface relative to the structure of an undistorted bilayer. The outlined black parallelogram shows the unit cell, and the displacements arrows are shown in red. (c) Wavefunctions of the lowest conduction band at the Gamma (Γ) point. The positive phase is shown in green, and the negative phase is shown in purple. (d-f) The imaginary dielectric function showing only contribution of the lowest conduction band of ReS_2 bilayer from (d) P_{up} interface, (e) P_{down} interface, and (f) pristine bilayer. The parallel (\parallel) direction is along the b -axis and the cross direction (\perp) is perpendicular to the b -axis.

CONCLUSION

We demonstrate the first non-volatile, electrically programmable control of optical anisotropy in a 2D material (ReS₂) through a back-gated FeFET employing ferroelectric AlScN, achieving record-breaking linear dichroism tunability ($\approx 95\%$) with retention times exceeding 12,000 seconds. The exfoliated ReS₂ exhibits distinct in-plane optical properties due to pseudo-1D Re-Re chains along the *b*-axis, as we confirm through polarization-resolved PL and differential reflectance measurements. The underlying mechanism—asymmetric charge transfer induced by ferroelectric polarization switching—provides fundamental insights into voltage-programmable material properties. Ferroelectric bound charges selectively populate ReS₂ electronic states in the P_{up} configuration and trigger structural distortions, while minimal charge transfer to ReS₂ occurs in the P_{down} state, thereby establishing the correlation between interfacial charge dynamics, structural perturbations, and anisotropic optical responses. Our study highlights the potential of ferroelectric gating for non-volatile, polarization-controlled optoelectronic devices, providing a versatile framework for engineering anisotropic properties in ReS₂ and similar 2D semiconductors for advanced, programmable photonic device applications.

EXPERIMENTAL PROCEDURES

Device fabrication

$\text{Al}_{0.68}\text{Sc}_{0.32}\text{N}$ with a thickness of 100 nm is deposited on pre-deposited Pt using a pulsed-DC reactive sputtering deposition system (Evatec, CLUSTERLINE 200 II pulsed DC PVD). (See details in Refs.^{25-27,38}) The co-sputtering process uses separate 4-inch Al and Sc targets, at a chuck temperature of 350 °C, with 10 sccm of Ar gas flow and 25 sccm of N_2 gas flow under the constant pressure of $\sim 1.45 \times 10^{-3}$ bar. The preferentially oriented (111) Pt layer promotes the growth of AlScN with highly textured ferroelectricity along the [0001] direction. Few-layer ReS_2 thin crystals (flakes) are mechanically exfoliated from the bulk crystal and then transferred onto AlScN/Pt substrates using a PDMS stamp under ambient conditions. Source and drain contact of Cr/Au (10/40 nm) are defined through e-beam lithography (Elionix ELS-7500EX). The Pt beneath the AlScN is used as a gate contact, where the gate contact region was exposed via wet etching of AlScN on the corner of the substrate by dipping it in the KOH solution post fabrication of the Au/Cr/ ReS_2 /AlScN/Pt heterostructure. No additional heat treatment is applied to the sample after device fabrication.

Device measurements

Room-temperature electrical measurements are performed in air at ambient temperatures in a Lakeshore probe station using a Keithley 4200A semiconductor analyzer. For the devices in **Figs. 2 and 3**, all the optical measurements are conducted after electrical programming/erasing at the probe station. The interval from applying the electrical signal for P_{up} and P_{down} states to conducting the optical measurement (including moving the sample and setting up the apparatus) is ≈ 5 min. During this transfer of sample, the sample was exposed to room temperature air. Optical measurements are carried out using a Horiba LabRam HR Evolution confocal microscope. A 633 nm (1.96 eV) continuous-wave laser serves as the excitation source for PL, and the white light source (AvaLight-HAL) was used for the reflectance measurement. For polarization-resolved PL and reflectance studies, a half-wave plate is used to control the polarization of linearly polarized excitation light, which is subsequently focused onto the sample. A 50 \times objective with $\text{NA} \approx 0.3$ is

used both for the sample excitation, and for capturing the emitted signal via an electron-multiplying charge coupled detector. For low-temperature PL measurements at 77 K, the samples are maintained on a cryogenic Linkam stage (THMS600) under a vacuum level of $\sim 10^{-3}$ Torr, and the temperature is lowered at a rate of ≈ 5 °C/min using a liquid nitrogen cryostat.

Theoretical calculations

Optimized atomic positions and electronic structures were obtained using density functional theory (DFT) as implemented in the Quantum Espresso software package^{39,40}. The exchange correlation energy is treated using the generalized gradient approximation of Perdew-Burke-Ernzerhof (PBE)⁴¹. A planewave basis set with a cutoff energy of 50 Ry for wavefunctions and 320 Ry for charge density was used, and the core electrons are represented using GBRV ultrasoft pseudopotentials⁴². Grimme's semi-empirical DFT-D3 dispersion correction is used to capture the van der Waals (vdW) interactions⁴³ between the ReS₂ layers. The Brillouin zone was sampled using a $4 \times 4 \times 1$ Monkhorst-Pack mesh. In calculations of the heterogeneous slab, the Fermi surface is treated using gaussian smearing with a value of 0.136 eV, and a dipole correction⁴⁴ was used to cancel the electric field in the vacuum region. Geometric relaxation of the interface structures was performed with a force convergence threshold of 0.026 eV/Å and a total energy convergence threshold of 0.0026 eV.

A denser k point grid of $12 \times 12 \times 1$ was used for density of states calculations. Optical spectra were calculated for the ReS₂ with structural distortions induced by charge transfer in the interface. The AlN and Pt layers were removed and the ReS₂ bilayer distortions were preserved. The occupations were fixed to include transitions into the lowest conduction band. The imaginary dielectric function was computed using momentum matrix elements obtained from the ground-state wavefunctions and charge density of the free standing ReS₂ bilayer. Wavefunctions were calculated non-self consistently on a denser $32 \times 32 \times 1$ k -point grid using a planewave cutoff of 50 Ry for the valence electrons and optimized norm-conserving pseudopotentials^{45,46} generated from OPIUM for the core electrons. A broadening parameter of 0.027 eV was used to obtain high resolution of the dielectric tensor. We calculate ϵ_2 according to Fermi's golden rule as written in Equation 1.

$$\varepsilon_2(\omega) = \frac{2\pi e^2}{\varepsilon_0 m^2 \omega^2} \int \frac{d\mathbf{k}}{(2\pi)^3} |\hat{\mathbf{a}}_0 \cdot \mathbf{P}_{fi}|^2 \delta[E_{fi}(\mathbf{k}) - \hbar\omega] \quad (1)$$

Where m is the electron mass, ω is the frequency of incident light, $\hat{\mathbf{a}}_0$ is a unit vector denoting the light polarization, \mathbf{P}_{fi} is an element of the interband momentum matrix (dipole matrix element), and E_{fi} is the energy difference between starting and ending bands i and f . A sum over all direct interband transitions between the occupied and unoccupied states was performed.

SUPPLEMENTAL INFORMATION

Fig S1-9, and Note S1.

ACKNOWLEDGMENTS

D.J., S.S. and M.R. acknowledge primary support for this work from the Office of Naval Research (ONR) Nanoscale Computing and Devices program (N00014-24-1-2131) and partial support from National Science Foundation (NSF) Future of Semiconductors (FuSe) program award number 2328743. D.J. and K-H.K. acknowledge support from the Air Force Office of Scientific Research (AFOSR) GHz-THz program grant number FA9550-23-1-0391. D.J., J.L. and B.C. acknowledge support from ONR Metamaterials program (N00014-23-1-2037). The materials modeling and theoretical spectroscopy of A.M.S. and A.M.R. were supported by the U.S. Department of Energy, Office of Science, Basic Energy Sciences, under Award No. DE-SC0024942. A.C.K. acknowledges the support of the National Science Foundation through the Graduate Research Fellowship Program (NSF-GRFP). A portion of the sample fabrication, assembly, and characterization were carried out at the Singh Center for Nanotechnology at the University of Pennsylvania, which is supported by the National Science Foundation (NSF) National Nanotechnology Coordinated Infrastructure Program grant NNCI-1542153. Computational support was provided by the National Energy Research Scientific Computing Center (NERSC), a U.S. Department of Energy, Office of Science User Facility located at Lawrence Berkeley National Laboratory, operated under Contract No. DE-AC02-05CH11231. This work was also supported by the Institute for Basic Science, South Korea (IBS-R036-D1), and through the National Research

Foundation (NRF) of Korea (Grant No. RS-2025-00516532) funded by the Ministry of Science and ICT.

AUTHOR CONTRIBUTIONS

M.R. and S.S. performed most of the experiments with assistance from B.C., K.-H.K., W.L., J.L., and H.S.S.. A.C.K. and A.M.S. performed the theoretical calculations under supervision of A.M.R. M.R. and S.S. wrote the manuscript, with input from A.C.K. All the authors revised and commented on the manuscript; D.J. and S.S. conceived, planned, and supervised the project. All authors contributed to the writing of the manuscript and interpretation of the data.

DECLARATION OF INTERESTS

The authors declare no competing interests.

References

- 1 Oka, K. & Kaneko, T. Compact complete imaging polarimeter using birefringent wedge prisms. *Opt. Express* **11**, 1510-1519 (2003). <https://doi.org/10.1364/OE.11.001510>
- 2 Nicholls, L. H. *et al.* Ultrafast synthesis and switching of light polarization in nonlinear anisotropic metamaterials. *Nature Photonics* **11**, 628-633 (2017). <https://doi.org/10.1038/s41566-017-0002-6>
- 3 Niu, S. *et al.* Giant optical anisotropy in a quasi-one-dimensional crystal. *Nature Photonics* **12**, 392-396 (2018). <https://doi.org/10.1038/s41566-018-0189-1>
- 4 Ermolaev, G. A. *et al.* Giant optical anisotropy in transition metal dichalcogenides for next-generation photonics. *Nature Communications* **12**, 854 (2021). <https://doi.org/10.1038/s41467-021-21139-x>
- 5 Ma, L.-L. *et al.* Self-assembled liquid crystal architectures for soft matter photonics. *Light: Science & Applications* **11**, 270 (2022). <https://doi.org/10.1038/s41377-022-00930-5>
- 6 Weber, M. F., Stover, C. A., Gilbert, L. R., Nevitt, T. J. & Ouderkirk, A. J. Giant Birefringent Optics in Multilayer Polymer Mirrors. *Science* **287**, 2451-2456 (2000). <https://doi.org/10.1126/science.287.5462.2451>
- 7 Edrington, A. C. *et al.* Polymer-Based Photonic Crystals. *Advanced Materials* **13**, 421-425 (2001). [https://doi.org/10.1002/1521-4095\(200103\)13:6<421::AID-ADMA421>3.0.CO;2-#](https://doi.org/10.1002/1521-4095(200103)13:6<421::AID-ADMA421>3.0.CO;2-#)
- 8 Shi, Z. *et al.* Continuous angle-tunable birefringence with freeform metasurfaces for arbitrary polarization conversion. *Science Advances* **6**, eaba3367 <https://doi.org/10.1126/sciadv.aba3367>
- 9 Shannon, R. D. & Fischer, R. X. Empirical electronic polarizabilities in oxides, hydroxides, oxyfluorides, and oxychlorides. *Physical Review B* **73**, 235111 (2006). <https://doi.org/10.1103/PhysRevB.73.235111>
- 10 Abedini Dereshgi, S. *et al.* Lithography-free IR polarization converters via orthogonal in-plane phonons in α -MoO₃ flakes. *Nature Communications* **11**, 5771 (2020). <https://doi.org/10.1038/s41467-020-19499-x>
- 11 Lomheim, T. S. & DeShazer, L. G. Optical-absorption intensities of trivalent neodymium in the uniaxial crystal yttrium orthovanadate. *Journal of Applied Physics* **49**, 5517-5522 (1978). <https://doi.org/10.1063/1.324471>
- 12 Dodge, M. J. Refractive properties of magnesium fluoride. *Appl. Opt.* **23**, 1980-1985 (1984). <https://doi.org/10.1364/AO.23.001980>
- 13 Butt, M. A., Khonina, S. N. & Kazanskiy, N. L. Recent advances in photonic crystal optical devices: A review. *Optics & Laser Technology* **142**, 107265 (2021). <https://doi.org/10.1016/j.optlastec.2021.107265>
- 14 Wang, S. *et al.* Two-dimensional devices and integration towards the silicon lines. *Nature Materials* **21**, 1225-1239 (2022). <https://doi.org/10.1038/s41563-022-01383-2>
- 15 Biswas, S., Grajower, M. Y., Watanabe, K., Taniguchi, T. & Atwater, H. A. Broadband electro-optic polarization conversion with atomically thin black phosphorus. *Science* **374**, 448-453 (2021). <https://doi.org/10.1126/science.abj7053>
- 16 Ma, W. *et al.* In-plane anisotropic and ultra-low-loss polaritons in a natural van der Waals crystal. *Nature* **562**, 557-562 (2018). <https://doi.org/10.1038/s41586-018-0618-9>

- 17 Li, X. *et al.* Review of Anisotropic 2D Materials: Controlled Growth, Optical Anisotropy Modulation, and Photonic Applications. *Laser & Photonics Reviews* **15**, 2100322 (2021). <https://doi.org/https://doi.org/10.1002/lpor.202100322>
- 18 Feng, Y. *et al.* Visible to mid-infrared giant in-plane optical anisotropy in ternary van der Waals crystals. *Nature Communications* **14**, 6739 (2023). <https://doi.org/10.1038/s41467-023-42567-x>
- 19 Choi, B. *et al.* Giant Optical Anisotropy in 2D Metal–Organic Chalcogenates. *ACS Nano* **18**, 25489-25498 (2024). <https://doi.org/10.1021/acsnano.4c05043>
- 20 Song, S., Rahaman, M. & Jariwala, D. Can 2D Semiconductors Be Game-Changers for Nanoelectronics and Photonics? *ACS Nano* **18**, 10955-10978 (2024). <https://doi.org/10.1021/acsnano.3c12938>
- 21 Yang, H. *et al.* Optical Waveplates Based on Birefringence of Anisotropic Two-Dimensional Layered Materials. *ACS Photonics* **4**, 3023-3030 (2017). <https://doi.org/10.1021/acsp Photonics.7b00507>
- 22 Aslan, B., Chenet, D. A., van der Zande, A. M., Hone, J. C. & Heinz, T. F. Linearly Polarized Excitons in Single- and Few-Layer ReS₂ Crystals. *ACS Photonics* **3**, 96-101 (2016). <https://doi.org/10.1021/acsp Photonics.5b00486>
- 23 Sherrott, M. C. *et al.* Anisotropic Quantum Well Electro-Optics in Few-Layer Black Phosphorus. *Nano Letters* **19**, 269-276 (2019). <https://doi.org/10.1021/acs.nanolett.8b03876>
- 24 Song, S. *et al.* High Current and Carrier Densities in 2D MoS₂/AlScN Field-Effect Transistors via Ferroelectric Gating and Ohmic Contacts. *ACS Nano* **19**, 8985-8996 (2025). <https://doi.org/10.1021/acsnano.4c17301>
- 25 Liu, X. *et al.* Aluminum scandium nitride-based metal–ferroelectric–metal diode memory devices with high on/off ratios. *Applied Physics Letters* **118** (2021). <https://doi.org/10.1063/5.0051940>
- 26 Liu, X. *et al.* Post-CMOS Compatible Aluminum Scandium Nitride/2D Channel Ferroelectric Field-Effect-Transistor Memory. *Nano Letters* **21**, 3753-3761 (2021). <https://doi.org/10.1021/acs.nanolett.0c05051>
- 27 Kim, K.-H. *et al.* Scalable CMOS back-end-of-line-compatible AlScN/two-dimensional channel ferroelectric field-effect transistors. *Nature Nanotechnology* (2023). <https://doi.org/10.1038/s41565-023-01399-y>
- 28 Lin, Y.-C. *et al.* Single-Layer ReS₂: Two-Dimensional Semiconductor with Tunable In-Plane Anisotropy. *ACS Nano* **9**, 11249-11257 (2015). <https://doi.org/10.1021/acsnano.5b04851>
- 29 Sim, S. *et al.* Ultrafast quantum beats of anisotropic excitons in atomically thin ReS₂. *Nature Communications* **9**, 351 (2018). <https://doi.org/10.1038/s41467-017-02802-8>
- 30 Jadcak, J. *et al.* Exciton binding energy and hydrogenic Rydberg series in layered ReS₂. *Scientific Reports* **9**, 1578 (2019). <https://doi.org/10.1038/s41598-018-37655-8>
- 31 Yu, Z. G., Cai, Y. & Zhang, Y.-W. Robust Direct Bandgap Characteristics of One- and Two-Dimensional ReS₂. *Scientific Reports* **5**, 13783 (2015). <https://doi.org/10.1038/srep13783>
- 32 Xia, F., Wang, H. & Jia, Y. Rediscovering black phosphorus as an anisotropic layered material for optoelectronics and electronics. *Nature Communications* **5**, 4458 (2014). <https://doi.org/10.1038/ncomms5458>

- 33 Yuan, H. *et al.* Polarization-sensitive broadband photodetector using a black phosphorus vertical p–n junction. *Nature Nanotechnology* **10**, 707-713 (2015). <https://doi.org/10.1038/nnano.2015.112>
- 34 Guo, Q. *et al.* Colossal in-plane optical anisotropy in a two-dimensional van der Waals crystal. *Nature Photonics* **18**, 1170-1175 (2024). <https://doi.org/10.1038/s41566-024-01501-3>
- 35 Zhang, H. *et al.* Cavity-enhanced linear dichroism in a van der Waals antiferromagnet. *Nature Photonics* **16**, 311-317 (2022). <https://doi.org/10.1038/s41566-022-00970-8>
- 36 Yasuoka, S. *et al.* Probing of Polarization Reversal in Ferroelectric (Al,Sc)N Films Using Single- and Tri-Layered Structures With Different Sc/(Al+Sc) Ratio. *Advanced Materials Interfaces* **12**, 2400627 (2025). <https://doi.org/https://doi.org/10.1002/admi.202400627>
- 37 Jhi, J.-H. C. a. S.-H. Origin of distorted 1T-phase ReS₂: first-principles study. *Journal of Physics: Condensed Matter* **30** (2018). <https://doi.org/10.1088/1361-648X/aaac95>
- 38 Kim, K.-H. *et al.* Tuning Polarity in WSe₂/AlScN FeFETs via Contact Engineering. *ACS Nano* **18**, 4180-4188 (2024). <https://doi.org/10.1021/acsnano.3c09279>
- 39 Giannozzi, P. *et al.* Advanced capabilities for materials modelling with QUANTUM ESPRESSO. *Journal of Physics: Condensed Matter* **29**, 465901 (2017).
- 40 Giannozzi, P. *et al.* QUANTUM ESPRESSO: a modular and open-source software project for quantum simulations of materials. *Journal of Physics: Condensed Matter* **21**, 395502 (395519pp) (2009).
- 41 Perdew, J. P., Ernzerhof, M. & Burke, K. Rationale for mixing exact exchange with density functional approximations. *The Journal of chemical physics* **105**, 9982-9985 (1996).
- 42 Garrity, K. F., Bennett, J. W., Rabe, K. M. & Vanderbilt, D. Pseudopotentials for high-throughput DFT calculations. *Computational Materials Science* **81**, 446-452 (2014). <https://doi.org/https://doi.org/10.1016/j.commatsci.2013.08.053>
- 43 Grimme, S., Antony, J., Ehrlich, S. & Krieg, H. A consistent and accurate ab initio parametrization of density functional dispersion correction (DFT-D) for the 94 elements H-Pu. *The Journal of Chemical Physics* **132** (2010). <https://doi.org/10.1063/1.3382344>
- 44 Bengtsson, L. Dipole correction for surface supercell calculations. *Physical Review B* **59**, 12301-12304 (1999). <https://doi.org/10.1103/PhysRevB.59.12301>
- 45 Rappe, A. M., Rabe, K. M., Kaxiras, E. & Joannopoulos, J. D. Optimized pseudopotentials. *Physical Review B* **41**, 1227-1230 (1990). <https://doi.org/10.1103/PhysRevB.41.1227>
- 46 Ramer, N. J. & Rappe, A. M. Designed nonlocal pseudopotentials for enhanced transferability. *Physical Review B* **59**, 12471-12478 (1999). <https://doi.org/10.1103/PhysRevB.59.12471>

Supplementary information for

Reconfigurable, non-volatile control of optical anisotropy in ReS₂ via ferroelectric gating

Mahfujur Rahaman^{1,†}, Seunguk Song^{1,2,3,†,*}, Aaliyah C. Khan⁴, Bongjun Choi¹, Aaron M. Schankler⁴, Kwan-Ho Kim¹, Wonchan Lee^{2,3}, Jason Lynch¹, Hyeon Suk Shin^{3,5}, Andrew M. Rappe⁴, and Deep Jariwala^{1*}

¹*Department of Electrical and Systems Engineering, University of Pennsylvania, Philadelphia, Pennsylvania 19104, United States*

²*Department of Energy Science, Sungkyunkwan University (SKKU), Suwon 16419, Republic of Korea*

³*Center for 2D Quantum Heterostructures (2DQH), Institute for Basic Science (IBS), Suwon 16419, Republic of Korea*

⁴*Department of Chemistry, University of Pennsylvania, Philadelphia, Pennsylvania 19104, USA.*

⁵*Department of Chemistry, Sungkyunkwan University (SKKU), Suwon, 16419, Republic of Korea*

[†]These authors contributed equally: Mahfujur Rahaman, Seunguk Song

*Correspondence should be addressed. Email to: seunguk@skku.edu (S.S.), dmj@seas.upenn.edu (D.J.)

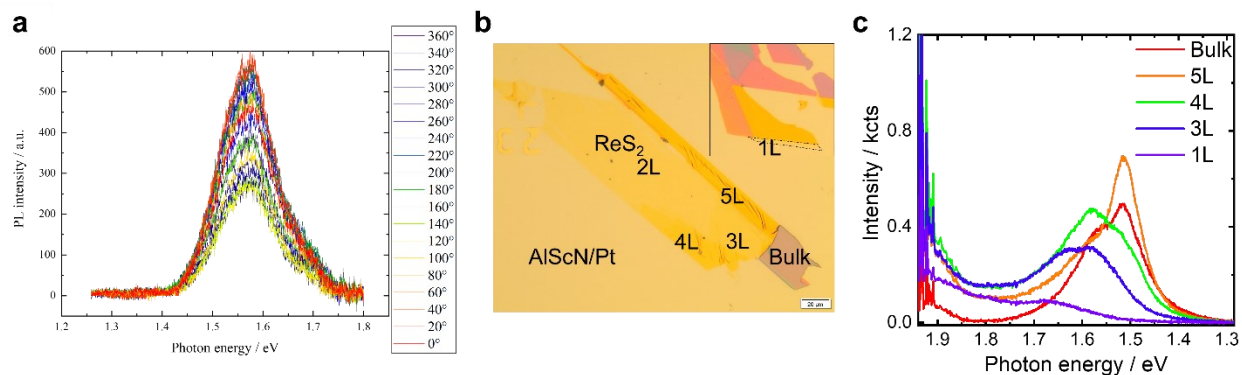


Figure S1. Raw PL data and flake thickness analysis of mechanically exfoliated ReS₂. (a) Raw polarized PL spectra presented in Figure 1d. A 633 nm solid-state laser with 100 μ W power is illuminated onto the sample to collect PL signal from the ReS₂ device. The light is focused onto the sample using 100x, 0.9 NA objective and the collected light was dispersed using 100 //mm groove grating. A $\lambda/2$ plate is placed onto the path of excitation to tune the polarization of excited light. Whereas the polarization state of the collected light was kept unchanged, perpendicular to the diffraction grating to have the maximum grating efficiency. The PL peak is centered at 1.57, representative of 3L ReS₂. (b) Optical image of ReS₂ flakes transferred on AlScN. PL measurements are used to determine the thickness of the ReS₂ flakes. (c) Thickness dependent PL spectra of ReS₂ flakes is shown in (b). According to literature^{1,2}, we can identify the thickness of ReS₂ flakes from monolayer to bulk using the PL peak positions.

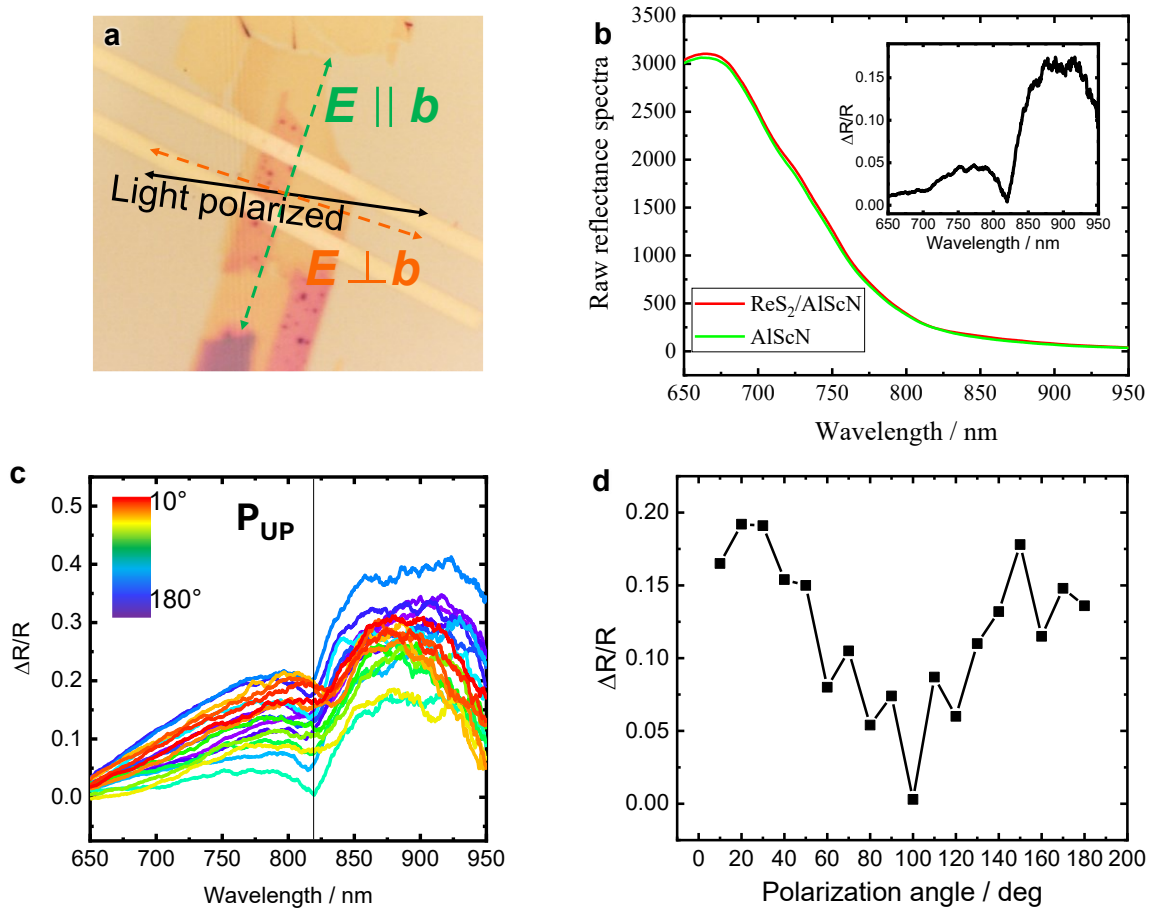


Figure S2. Angle-dependent differential reflectance spectra under ferroelectric switching. (a) Optical micrograph of the ReS₂/AlScN FeFET investigated in Fig. 2a. The crystallographic a-axis (green dashed line) and b-axis (red dashed line) are indicated relative to the incident electric-field vector (E_0 , black line) at 0° polarizer orientation. The polarizer is then rotated clockwise in 10° steps from 0° to 180°, and a reflectance spectrum was collected at each angle. (b) Representative raw reflectance spectra of ReS₂/AlScN (orange) and the bare AlScN reference (grey) acquired at a polarizer angle of 100° after applying a positive gate bias. The inset shows the corresponding differential reflectance, $\Delta R/R$. (c) Differential reflectance spectra $\Delta R/R$ for all polarization angles (0–180°, 10° step) in the P_{up} state, illustrating the strong anisotropy of ReS₂. (d) Polar plot of the differential reflectance intensity at 820 nm (near the ReS₂ bandgap) as a function of polarization angle, demonstrating tunable optical modulation via polarization control.

Figure S2a shows the ReS₂ device under study (discussed in **Fig. 2a**). Both ReS₂ axis are sketched with respect to the optical field and shown with green and red dashed lines respectively. Incoming optical field (incident light field) at zero degree of the polarizer is shown by the black straight line on the image. We gradually rotate the angle of the polarizer clockwise with a step of 10 degree

and collect reflectance spectra for each step. **Figure S2b** presents raw reflectance spectra of ReS₂/AlScN and AlScN reference substrate for a polarization angle of 100° measured after the device is positively biased (P_{up} state). To determine the differential reflectance spectra, we use the following formula:

$$\Delta R = \frac{R_{ReS2/AlScN} - R_{AlScN}}{R_{AlScN}}$$

Where $R_{ReS2/AlScN}$ and R_{AlScN} are the polarization angle-dependent raw reflectance spectra. **Inset of Fig. S2b** shows the differential reflectance spectra determined at polarization angle of 100°. Using this method, we determine the differential reflectance spectra of the device for a varying angle between zero degree to 180°. All the Differential reflectance spectra measured under positive bias (P_{up}) are displayed in **Fig. S2c**. **Figure S2d** plotted the differential reflectance intensity of the device as a function of polarization angle measured at the ReS₂ bandgap at 820 nm. As can be seen, we can modulate the reflectance via tuning the polarization angle of the incident light.

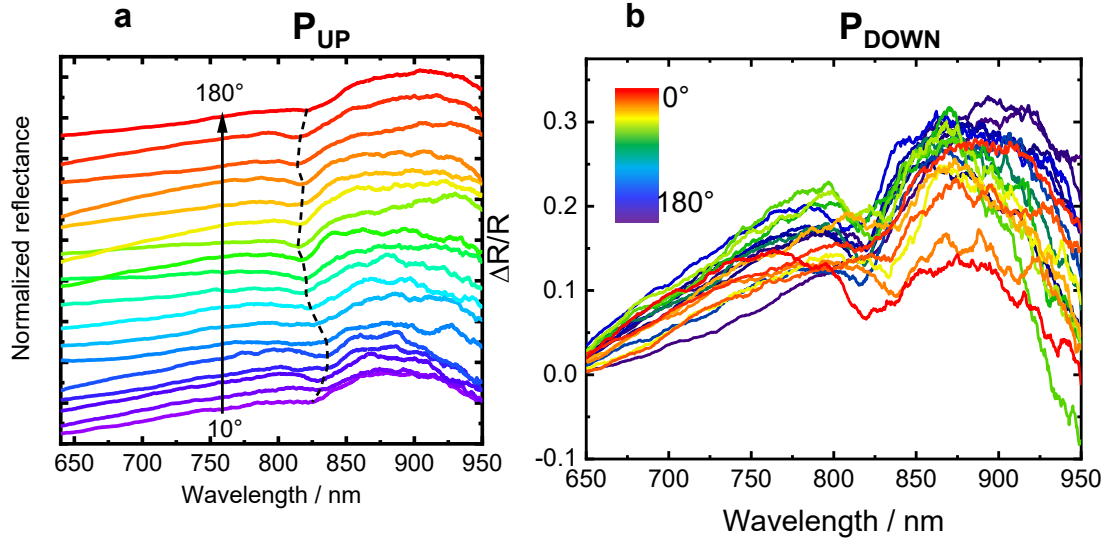


Fig. S3. Polarization-sensitive exciton response of ReS₂ near the band edge. (a) Normalized differential reflectance spectra of the ReS₂/AlScN FeFET (from Fig. S2c) under positive bias (P_{up}), showing polarization-angle-dependent spectral modulation around the bandgap. Two dominant excitonic features, X_1 and X_2 , exhibit varying spectral weights with polarization. (b) Differential reflectance spectra of the same device under negative bias (P_{down}), as a function of incident light polarization angle. Similar polarization-sensitive behavior of excitonic features is observed, indicating that the optical anisotropy of ReS₂ persists across polarization states.

ReS₂ has multiple excitation channels around bandgap. Two prominent excitonic features are X_1 and X_2 (Ref.^{1,2}). As reported in literature, these two excitonic features have different linear polarization sensitivity. As a result, the spectral weight of these excitons varies as the polarization angle of the incident light changes. We also observed similar behavior in our polarization angle dependent reflectance spectra. **Figure S3a** presents normalized differential reflectance spectra of the ReS₂ device presented in **Fig. S2c**. As can be seen, with the change of polarization angle of incident light the shape of the reflectance spectra around the bandgap also changes indicative of the change of spectral weight of the excitons X_1 and X_2 . **Figure S3b** displays polarization angle dependent differential reflectance spectra of the ReS₂ device discussed in **Fig. S2a** and **Fig. 2** in the main text under negative bias.

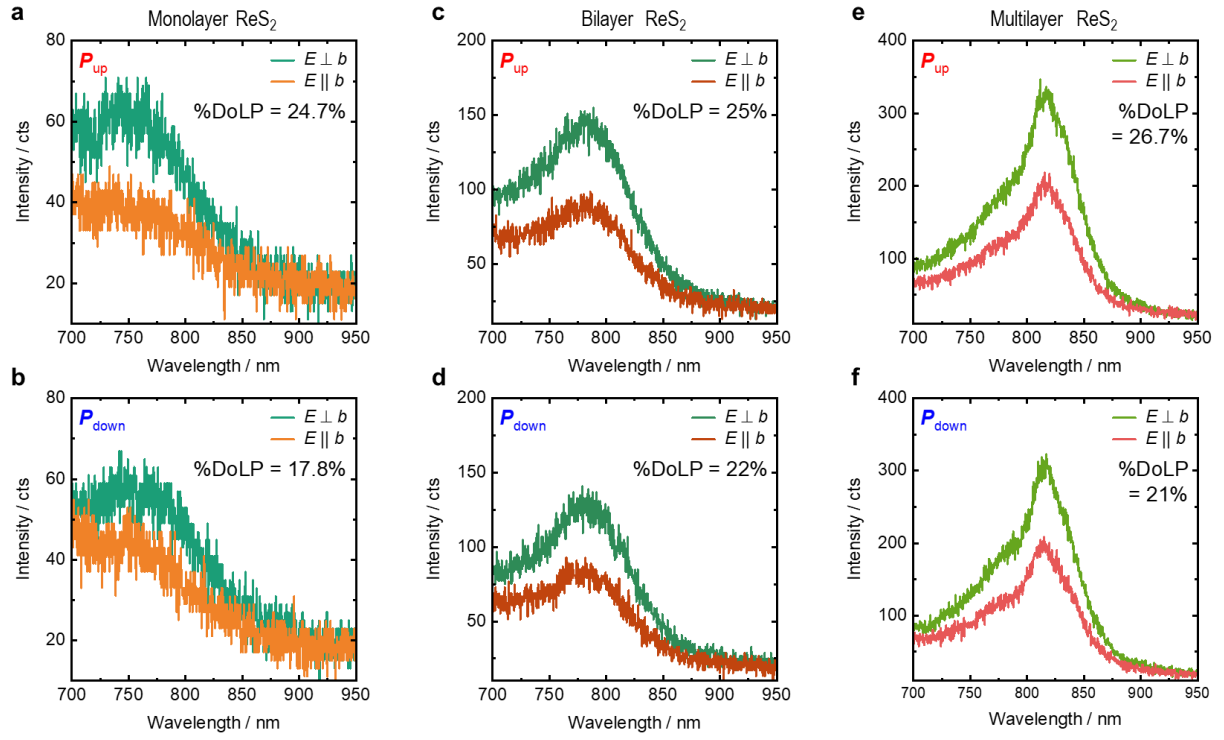


Figure S4. Thickness-independent DoLP modulation in ReS_2 at room temperature. Monolayer, bilayer, and multilayer devices all exhibit a consistently higher degree of linear polarization in the P_{up} state (~24.7-26.7 %) than in the P_{down} state (~17-22 %), confirming reproducibility across layer numbers.

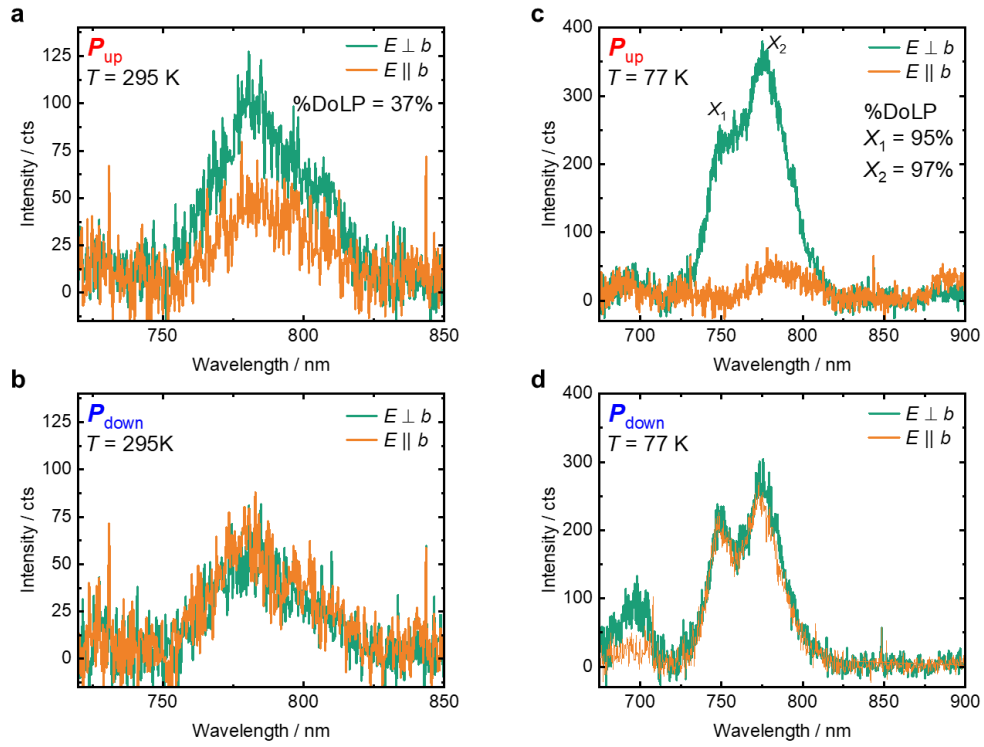


Figure S5. Polarization-resolved PL spectroscopy. (a, b) Room-temperature polarization-resolved PL spectra of the ReS₂/AlScN FeFET for the (a) P_{up} and (b) P_{down} states. (c, d) Normalized polarization-resolved PL spectra measured at ≈ 77 K for the (c) P_{up} and (d) P_{down} states.

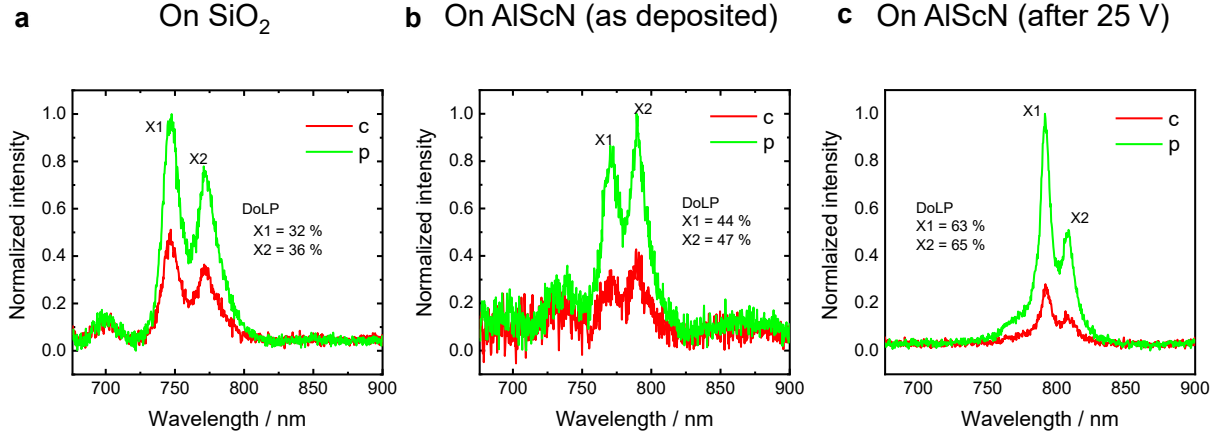


Figure S6. Substrate-dependent polarization-resolved photoluminescence. (a) Linearly polarized PL spectra of a 5-layer ReS_2 flake on a SiO_2 substrate at 77 K. Spectra collected with polarization parallel (green) and perpendicular (red) to the ReS_2 b -axis reveal distinct polarization-dependent excitonic features. (b) Linearly polarized PL spectra of an as-deposited 5-layer ReS_2 flake on an AlScN under identical measurement conditions, prior to device fabrication. A modest increase in the DoLP is observed compared to the SiO_2 case due to the partial polarization of AlScN. (c) Linearly polarized PL spectra of the same ReS_2 flake after device fabrication under a positive gate bias (corresponding to Fig. 3 in the main text), highlighting further modulation of excitonic polarization response.

Figure S6a-c presents comparative study of polarization sensitivity of ReS_2 excitons on different substrates. All the PL spectra are collected at 77 K. **Figure S6a** shows the linearly polarized PL spectra of 5L ReS_2 flake on SiO_2 substrate. Here, green (red) spectra are collected parallel (perpendicular) to the ReS_2 b axis. **Figure S6b** shows linearly polarized PL spectra of as deposited 5L ReS_2 flake on AlScN substrate. The PL spectra presented in **Fig. S6b** are collected before the device fabrication. Comparing the DoLP of ReS_2 on SiO_2 and AlScN substrates we observed a small increase of DoLP on AlScN substrate for as deposited ReS_2 flake. AlScN is well-known for its intrinsically net positive polarization states (i.e., partial polarization)³. Therefore, our hypothesis for this small increase of DoLP for as deposited ReS_2 on AlScN is that net small positive polarization of AlScN results in small increase in DoLP. For comparison linear polarized PL spectra of ReS_2 device discussed in **Fig. 3** in the main text under positive bias are also included in **Fig. S6c**.

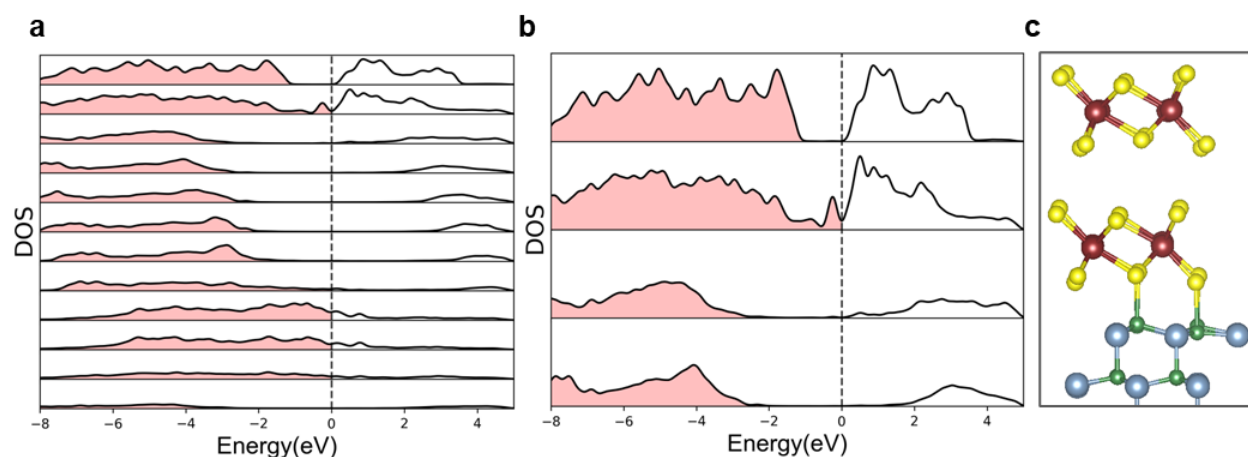


Figure S7. Layer-resolved electronic structure and interfacial charge transfer in the P_{up} interface. (a) Layer projected density of states (LPDOS) for relaxed P_{up} interface, showing 12 layers going from 4 Pt layers at the bottom, 6 AlN layers in the middle, and two ReS₂ layers on top. The Fermi level is set to zero and is indicated by a black dashed line. (b) LPDOS of the ReS₂ bilayer and top two AlN layers only to show that the top layer of ReS₂ is relatively unaffected and charge is transferred only to the layer closest to the AlN. (c) Schematic of the ReS₂ and interacting AlN layers corresponding to the LPDOS in (b).

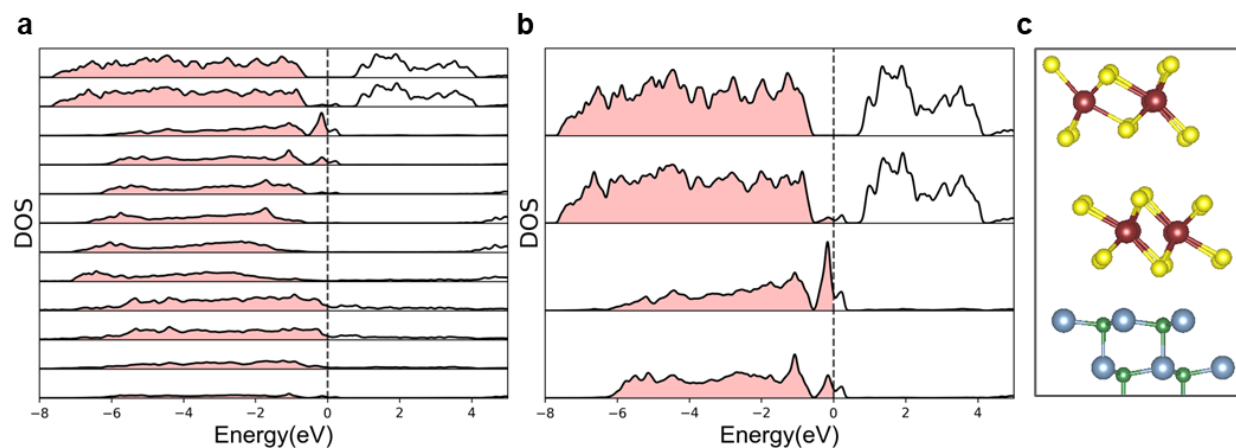


Figure S8. Layer-resolved electronic structure and interfacial charge transfer in the P_{down} interface. (a) Layer projected density of states (LPDOS) for relaxed P_{down} interface, showing 12 layers going from 4 Pt layers at the bottom, 6 AlN layers in the middle, and two ReS₂ layers on top. The Fermi level is set to zero and is indicated by a black dashed line. (b) LPDOS of the ReS₂ bilayer and top two AlN layers only to show that ReS₂ interface layer does not undergo charge transfer. (c) Schematic of the ReS₂ and AlN layers corresponding to the LPDOS in (b).

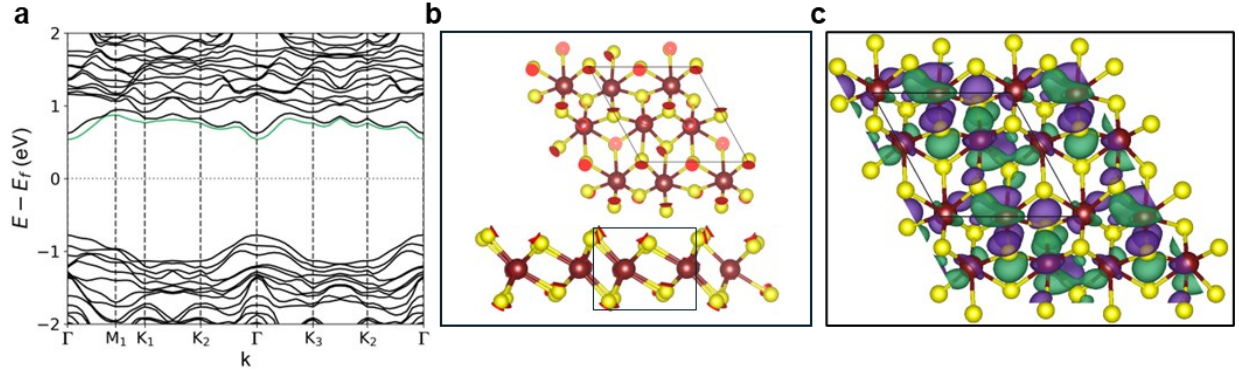


Figure S9. Theoretical analysis on charge induced distortion in P_{down} interface. (a) Electronic band structure of the ReS_2 bilayer with structural distortions from P_{down} interface highlighting the lowest conduction band (CBM) in green. (b) In-plane and side views (Re: red, S: yellow) of displacement pattern of the lowest ReS_2 layer in the P_{down} interface relative to the structure of an undistorted bilayer. The outlined black parallelogram shows the unit cell, and the displacements arrows are shown in red. (c) Wavefunctions of the lowest conduction band at the Γ point. The positive phase is shown in green, and the negative phase is shown in purple.

Supplementary Note S1. Theoretical modeling and interface analysis

A model system was constructed to theoretically rationalize the observed difference in optical response due to the polarization up (P_{up}) and down (P_{down}) states of AlScN in the device. A vertically stacked heterostructure was modeled to capture charge transfer and structural changes in the ferroelectric and the ReS₂ semiconductor layers of the device. The following guidelines were used in developing a simplified model of the device architecture: (i) Sc doping of AlN serves to lower the coercive field, making ferroelectricity viable in AlN. Therefore, we use pure AlN in our model for simplicity and to accurately represent how the two polar states influence the optoelectronic properties. (ii) The ReS₂ layer in the device is much thinner than the ferroelectric layer, so we model a bilayer of ReS₂ and 6 layers of AlN. (iii) The modulation of the optical response of ReS₂ is primarily due to its interaction with the up and down polarization states of the ferroelectric. We build a simplified model with ReS₂ and AlN and add a Pt layer below the AlN to passivate the bottom AlN surface and screen the depolarization field. The final structure was obtained with the following specifications. The topmost layer consists of bilayer ReS₂ (001). The middle layer is pure AlN in either its P_{up} or P_{down} polar wurtzite structure. A 6-layer slab of AlN was chosen, as it proved to be sufficient to stabilize the polar state. Finally, a bottom layer of Pt acts as an electron reservoir and screens the depolarization field of the ferroelectric. The in-plane lattice parameters of the AlN, and Pt are matched to those of the ReS₂ (001) bilayer which is a rhombohedral cell with $b = 6.40 \text{ \AA}$, $a = 6.5 \text{ \AA}$. The slabs are separated by 20 \AA of vacuum to avoid interactions between periodic images. Two total slab models (referred to as interfaces in main text) were created using the P_{up} or P_{down} AlN structures.

Supplementary References

- 1 Yu, Z. G., Cai, Y. & Zhang, Y.-W. Robust Direct Bandgap Characteristics of One- and Two-Dimensional ReS₂. *Scientific Reports* **5**, 13783 (2015). <https://doi.org/10.1038/srep13783>
- 2 Aslan, B., Chenet, D. A., van der Zande, A. M., Hone, J. C. & Heinz, T. F. Linearly Polarized Excitons in Single- and Few-Layer ReS₂ Crystals. *ACS Photonics* **3**, 96-101 (2016). <https://doi.org/10.1021/acsphotonics.5b00486>
- 3 Yasuoka, S. *et al.* Probing of Polarization Reversal in Ferroelectric (Al,Sc)N Films Using Single- and Tri-Layered Structures With Different Sc/(Al+Sc) Ratio. *Advanced Materials Interfaces* **12**, 2400627 (2025). [https://doi.org:https://doi.org/10.1002/admi.202400627](https://doi.org/https://doi.org/10.1002/admi.202400627)